Nat Hazards (2015) 78:1197–1224
DOI 10.1007/s11069-015-1765-z

ORIGINAL PAPER

Water–sediment flow modeling for field case studies in Southwest China

Ridong Chen[1] · **Songdong Shao**[2] · **Xingnian Liu**[1]

Received: 28 June 2014 / Accepted: 13 April 2015 / Published online: 24 April 2015

Abstract This paper presents a highly robust numerical model to simulate water–sediment mixture flows in practical field studies. The model is composed of an integrated algorithm combining the finite element characteristic splitting method and finite volume Godunov scheme. The former maintains the generality and stability of the numerical algorithm, while the latter ensures the conservation and accuracy of the model. The proposed model is first tested by three benchmark flow problems including flood flow in a pool, dam break over a mobile bed, and morphological process of a dam removal. Then, the model is applied to two practical field case studies to demonstrate its potential engineering values. The first case study is related to the damage of the Polo Hydropower Plant by a sediment flooding event. The second one is the investigation of a well-known 2013 dam-break flooding that happened in the Tangjiashan Mountain. It is shown that the simulated water and sediment flows are in good agreement with the documented laboratory and field data, and the numerical model is capable of providing useful information on the flow predictions, thus making further engineering measures to mitigate these disasters.

Keywords Water–sediment flow modeling · Southwest China · Flood · Sediment · Field study · Polo Hydropower Plant · Tangjiashan Mountain flood

✉ Xingnian Liu
scucrs@163.com

Ridong Chen
chenridong1984@163.com

Songdong Shao
s.shao@sheffield.ac.uk

[1] State Key Laboratory of Hydraulics and Mountain River Engineering, College of Water Resource and Hydropower, Sichuan University, Chengdu 610065, China

[2] Department of Civil and Structural Engineering, University of Sheffield, Sheffield S1 3JD, UK

1 Introduction

In China, there are around 50,000 rivers with a coverage area being 100 km^2 and 1500 rivers with a coverage area being 1000 km^2. Severe flood and sediment movement are typical features of these rivers due to soil erosion in the catchment area, which caused serious engineering concerns; especially, the Southwest China region is characterized by mountainous topography and narrow valley, and thus, quite a few large hydropower plants have been built to exploit the natural water resource. These dam constructions brought great benefit to the local economy, but meanwhile they also adversely influenced the balance between flow and sediment coexistences. In this sense, timely and accurate predictions of the flood and sediment flows could provide important information in the engineering field. However, the rivers in Southwest China mostly demonstrate large variation in the water levels and sediment transport capacities. In addition, the mobile bed is composed of different sizes of sediment materials, which made the process of bed evolution much more complex. Therefore, the development of an efficient and accurate numerical model for these mountainous rivers involves much more challenging tasks than those encountered in the plain rivers.

The accuracy of any water–sediment mixture flow models should rely on the underlying sediment mechanics. For example, Wang and Song (1995) summarized the sediment research status in Europe and America around the twentieth century, and Wang (1999) reviewed the river sedimentation issues in China. In recent years, great progresses have been made in the study of various sediment mechanics such as the transport capacity, bed form, and resistance. For example, 1D numerical models have been efficiently used for the simulation of flow and sediment processes across large spatial and temporal domains, including the CRS-1 model developed by Liu (2004) at Sichuan University and the HEC model developed by USACE (2003). In order to obtain more detailed flow information along the cross-sectional area, a variety of 2D numerical models have been developed (Demirbilek and Nwogu 2007), including the SMS model by Brigham University, RIVCOM by the Delft, and MKE21 by the DHI. As these 2D water–sediment flow models are very CPU-efficient and meanwhile can achieve sufficient accuracy in the flow simulations, they have been widely used in the engineering practice. In comparison, more complicated 3D models are often used in some refined areas for the purpose of theoretical study and model verification (Liu et al. 2012a, b). Most of the 2D numerical models are based on the hydrodynamic equations together with different sediment transport modes, in which the 2D shallow-water equations (SWEs) model could be the most widely adopted for large-scale river simulations. On the other hand, the commonly used numerical solution schemes are the finite difference method (FDM), finite element method (FEM), and finite volume method (FVM), respectively, to discretize the flow and sediment equations. Each numerical scheme has some kinds of advantage in certain flow problems but may not perform satisfactorily in a different situation. As a result, the combined or mixed solution schemes have been developed to deal with more complicated issues, such as the FEM-based FVM, FVM-based FEM, and hybrid FDM/FVM methods (Guillou and Nguyen 1999; Du 2000; Casulli and Zanolli 2002).

In order to investigate the practical sediment-laden flood flows in the field of Southwest China, we should have a competent numerical model that is not only stable and efficient, but also able to deal with complicated boundaries arising from the sediment transport and alluvial deformation. The FEM-based characteristic splitting method and FVM-based Godunov scheme have proved to be robust modeling techniques in numerous flow

applications, and thus, we will develop a hybrid numerical algorithm by combining the above two. The former guarantees the generality and stability of the solution scheme, while the latter ensures the conservation and accuracy of the model. The hybrid model will be used to simulate two field cases related to sediment flooding in the Southwest China, and the computational findings could provide useful information to mitigate the natural disasters in engineering practice.

2 Water–sediment mixture flow model

In the field of water–sediment mixture flow modeling, great achievements have been made in the fundamental equations to describe the physical process and the numerical schemes to solve these equations. Any robust numerical algorithm should not only possess the property of compatibility, stability, and convergence, but also demonstrate the feature of conservation, non-dissipation/dispersion, and computational efficiency/accuracy. In this section, first we introduce the governing equations in 2D domain for the water–sediment mixture flow, and then, the numerical solution technique using the FEM characteristic splitting method and FVM Godunov scheme is developed. The hybrid numerical algorithm inherited the advantages of both FEM and FVM and improved the numerical treatment of advection term.

2.1 Governing equations for water–sediment mixture flow

The following 2D shallow water equations (SWEs), sediment transport, and bed deformation equations are used for the water–sediment mixture flows as

$$\frac{\partial \eta}{\partial t} + \nabla \cdot (h\mathbf{u}) = 0 \tag{1}$$

$$\frac{\mathrm{d}(h\mathbf{u})}{\mathrm{d}t} = A_{\mathrm{H}} h \nabla^2 \mathbf{u} - gh\nabla\eta - \frac{gn^2|\mathbf{u}|\mathbf{u}}{h^{1/3}} \tag{2}$$

$$\frac{\mathrm{d}(hS)}{\mathrm{d}t} = \alpha\omega(S^* - S) + A_{\mathrm{H}} h \nabla^2 S \tag{3}$$

$$(1-\xi)\frac{\partial z_b}{\partial t} + \nabla \cdot \mathbf{q_b} = \frac{\alpha\omega(S - S^*)}{\rho_s} \tag{4}$$

in which η = water surface; t = time; h = flow depth; $\mathbf{u} = (u, v)$ are the horizontal 2D flow velocities; n = bed roughness; g = gravitational acceleration; S = sediment suspended load concentration; ω = sediment settling velocity; S^* = maximum suspended load-carrying capacity; α = erosion–deposition coefficient (0.25 is used for deposition, 1.0 for erosion, and 0.5 for transition); z_b = movable bed layer thickness; ξ = bed porosity; ρ_s = density of sediment grain; and $\mathbf{q}_b = (q_{bx}, q_{by})$ are the horizontal 2D sediment bed load transport in x- and y-directions.

Here, it should be noted that the above water flow Eqs. (1–2) are not influenced by any sediment transport parameters in Eqs. (3–4), and thus, they are represented in the uncoupled form, which is in contrast to those used by Cao et al. (2011). This is based on the rational that the suspended load is not the dominant sediment transport mode in the present

field case studies, and the flow structure is not significantly modified by the existence of the sediment mixture.

The horizontal eddy viscosity coefficient A_H in Eqs. (2) and (3) is represented as

$$A_H = C_s A\left[\left(\frac{\partial u}{\partial x}\right)^2 + 0.5\left(\frac{\partial v}{\partial x} + \frac{\partial u}{\partial y}\right)^2 + \left(\frac{\partial v}{\partial y}\right)^2\right]^{0.5} \tag{5}$$

in which C_s = Horcon coefficient, taken between 0.1 and 0.2 in this paper; and A = node influence area.

2.2 Evaluations of relevant sediment parameters

The choice of bed load transport equation is a difficult issue, as different formulations can predict the results within an error of several orders. Besides, the sediment bed load transport is also highly sensitive to the flow velocity, as the relationship between the two is not a linear function. Thus, unrealistic bed deformations can be predicted if the formula is not correctly used. In this study, we will adopt the widely used Meyer–Peter formula as follows:

$$\mathbf{q}_b = 8\sqrt{(s-1)g d_i^3}\,\frac{\mathbf{u}}{|\mathbf{u}|}\max(\tau_* - \tau_c, 0)^{1.5} \tag{6}$$

in which s = relative density of the sediment grain to water; d_i = sediment grain size of one group; $\tau_* = \frac{n^2|\mathbf{u}|^{1.5}}{(s-1)d_i h^{1/3}}$ is the flow shear stress; and $\tau_c = 0.047$ is the threshold shear stress of grain initiation. As the Meyer–Peter formula covered a relatively wide range of sediment grain sizes, it should be suitable for the field studies in Southwest China, in which most of the riverbeds are covered by the highly graded sediment materials.

The threshold grain size separating the bed load and suspended load materials can be determined by the so-called suspension index, which is represented by Qian and Wan (1983)

$$Rz = \frac{\omega}{\kappa u_*} \tag{7}$$

in which $\kappa = 0.41$ is the von Karmon constant and u_* = frictional velocity. From the case studies on many field rivers in the Southwest China, the general guidelines stipulate that $Rz > 4.166$ falls into the bed load and $Rz < 4.166$ belongs to the suspended load (Liu et al. 1991).

The sediment settling velocity is calculated by the following formula (Zhang 1961)

$$\omega = \sqrt{\left(13.95\frac{\upsilon}{d}\right)^2 + 1.09\frac{\gamma_s - \gamma}{\gamma}gd} - 13.95\frac{\upsilon}{d} \tag{8}$$

where υ = kinematic viscosity of water; γ_s and γ = gravity density of sediment grain and water, respectively.

The general form of sediment-carrying capacity of the flow can be represented by

$$S^* = k\left(\frac{U^3}{gh\omega}\right)^m \tag{9}$$

in which k and m = empirical sediment coefficients, whose values depend on the particular

river location. In practical sediment simulations, to address the non-uniformity of suspended load transport and the bed materials adjustment arising from the alluvial deformation, adequate modifications of Eq. (9) are provided by Zhang (1998).

3 Numerical solution schemes

Here, the proposed numerical solution method couples the FEM characteristic splitting with FVM Godunov schemes to improve the computational efficiency and accuracy. To improve the solution stability of advection-dominated flows, Zienkiewicz and Codina (1995) developed the split characteristic-based FEM scheme. This algorithm has the advantage of simplicity and stability and is particularly suitable for the simulation of mountainous river flows over relatively steep slope and complicated alluvial topographies. By following Zienkiewicz and Codina (1995), the split schemes in both the spatial and temporal domains are considered in this work.

On the other hand, the FVM-based Godunov scheme is widely used to solve the SWE-type equations of nonlinear hyperbolic feature due to its well-balanced conservation property (Pu et al. 2012). Thus, it can compensate for the drawback of FEM that cannot achieve the exact property conservation in all of the computational elements. Numerical schemes based on the Godunov are also quite efficient to treat the flows with large energy gradient as well as shock waves. By combining with the approximate Riemann solver, the computational efficiency is greatly improved when solving the momentum flux across the cells, and higher-order schemes can be easily implemented as a result.

In the coupled FEM–FVM computations, the FVM Godunov scheme is used to correct the deficiency cells except those on the boundaries after several time steps of FEM computation. So the conservation property of FEM scheme can be maintained by the coupled FVM scheme. Besides, the FEM uses a first-order accurate element, while the coupled model adopts the TVD algorithm which is second-order accurate. As the FEM and FVM methods use different storage systems to save the flow variables, frequent data interpolation and communication should be implemented to transfer the flow information between the two. A brief review of the coupled FEM–FVM solution procedure is provided below.

The solution of water flow is first carried out based on the FEM scheme. Let $\mathbf{R} = \begin{bmatrix} hu \\ hv \end{bmatrix}$, $\mathbf{r} = \begin{bmatrix} u \\ v \end{bmatrix}$, $\mathbf{q}_b = \begin{bmatrix} q_{bx} \\ q_{by} \end{bmatrix}$, and $\mathbf{i} = \begin{bmatrix} i_x \\ i_y \end{bmatrix}$, in which i_x and i_y are the slopes of the terrain, and then, the solution procedure of matrix $\mathbf{R}^{n+1}$ is

1. First step: Solving the variation in velocity $\Delta\mathbf{R}^*$

$$\Delta\mathbf{R}^* = \mathbf{R}^* - \mathbf{R}^n = -\mathbf{M}^{-1}\Delta t[(\mathbf{CR} + \mathbf{K_m r} - \mathbf{f}) - \Delta t(\mathbf{K_s R} + \mathbf{f_s})]^n \tag{10}$$

2. Second step: Solving the variation in depth $\Delta\mathbf{h}$

$$\Delta\mathbf{h} = \mathbf{M^{-1}}\Delta\mathbf{t}[\mathbf{H}(\mathbf{R^n} + \theta_1\Delta\mathbf{R}^*) - \Delta\mathbf{t}\theta_1\mathbf{G}\mathbf{p^n} - \mathbf{f_h}] \tag{11}$$

3. Third step: Using $\Delta\mathbf{h}$ and correcting $\Delta\mathbf{R}^*$ to get the value at next time step t^{n+1}

$$\mathbf{h^{n+1}} = \mathbf{h^n} + \Delta\mathbf{h} \tag{12}$$

$$\mathbf{R}^{n+1} = \mathbf{R}^n + \Delta\mathbf{R}^* - \mathbf{M}^{-1}\Delta t\mathbf{H}^T\mathbf{p}^n \tag{13}$$

The detailed definitions of relevant variables in Eqs. (10–13) can be found in Chen et al. (2011), so they are not repeated here. The computational time step should satisfy the following Courant criterion

$$\Delta t \le C_{\mathrm{FL}} \frac{l_{\mathrm{em}}}{c + |\mathbf{u}|} \tag{14}$$

in which l_{em} = characteristic element size; $c = \sqrt{gh}$ is the gravity wave celerity in shallow water; and C_{FL} = Courant stability coefficient, taken as 0.3–0.7 in the present paper.

4. Fourth step: Then, the FVM Godunov scheme is applied to improve the FEM performance, and the flow velocity field is updated by

$$\mathbf{u}_i^p = \mathbf{u}_i^n - \frac{\Delta t}{A_i}\sum_{j=1}^{3}\left(\mathbf{F}\cdot n_x + \mathbf{G}\cdot n_y\right)l_j \tag{15}$$

$$\mathbf{u}_i^{n+1} = \mathbf{u}_i^p + \Delta t S(\mathbf{u}_i^p) \tag{16}$$

in which p represents the prediction step; $\mathbf{F}$ and $\mathbf{G}$ = numerical flux in x- and y-directions, respectively; l = side length of the FV; and S = source term. The numerical flux can be calculated by the general HLLC schemes as

$$\mathbf{F}_{i+\frac{1}{2}}^{hllc} = \begin{cases} \mathbf{F}_{\mathrm{L}} & 0 \le S_{\mathrm{L}} \\ \mathbf{F}_{*\mathrm{L}} & S_{\mathrm{L}} \le 0 \le S_*, \mathbf{F}_{*\mathrm{L}} = \mathbf{F}_{\mathrm{L}} + S_{\mathrm{L}}(\mathbf{u}_{*\mathrm{L}} - \mathbf{u}_{\mathrm{L}}) \\ \mathbf{F}_{*\mathrm{R}} & S_* \le 0 \le S_{\mathrm{R}}, \mathbf{F}_{*\mathrm{R}} = \mathbf{F}_{\mathrm{R}} + S_{\mathrm{R}}(\mathbf{u}_{*\mathrm{R}} - \mathbf{u}_{\mathrm{R}}) \\ \mathbf{F}_{\mathrm{R}} & 0 \ge S_{\mathrm{R}} \end{cases} \tag{17}$$

in which $S_{\mathrm{L}} = u_{\mathrm{L}} - q_{\mathrm{L}}\sqrt{gh_{\mathrm{L}}}$, $S_* = u_*$, and $S_{\mathrm{R}} = u_{\mathrm{R}} + q_{\mathrm{R}}\sqrt{gh_{\mathrm{R}}}$. Besides, the accuracy of numerical scheme is further improved by applying the WAF TVD algorithm on the FV surface for flux computations.

5. Last step: Finally, the FEM solution procedure is applied again to solve the sediment transport equation and bed deformation equation as below [more detailed derivations can be referred to Chen et al. (2011)]

$$\mathbf{S}^{\mathbf{n+1}} = \mathbf{S}^{\mathbf{n}} - \mathbf{M}^{-1}\Delta\mathbf{t}(\mathbf{CS} + \mathbf{K_m S} - \mathbf{f})^{\mathbf{n}} + \mathbf{M}^{-1}(\Delta\mathbf{t})^{\mathbf{2}}(\mathbf{K_s S} + \mathbf{f_s})^{\mathbf{n}} \tag{18}$$

$$\mathbf{z_b^{n+1}} = \mathbf{z_b^n} - \frac{\mathbf{1}}{\mathbf{1}-\xi}(\mathbf{Hq_b} + \mathbf{f_c}) \tag{19}$$

4 Model verifications

4.1 Flood flow in a horizontal 2D water tank

This model test is based on the benchmark unsteady flow experiment carried out in the Spanish CITEEC laboratory by J. Puertas (Brufau et al. 2004). The computational domain is composed of two rectangular water tanks that are connected by a sluice gate, and the rest parts are solid walls. The upstream tank contains reservoir water, and the downstream tank is the flooded area, which also has a triangular barrier placed on one side of the wall to

generate complex geometry and flow conditions. The bed roughness of the whole computational domain is $n = 0.018$. The initial water depth in the upstream tank is 0.5 m, as compared with 0.1 m in the downstream area. The lift of the sluice gate is assumed to be instantaneous. Here, we will use the numerical simulations to reproduce the unsteady flooding process. The general layout of the computational domain with the location of six measurement points and the computational meshes is shown in Fig. 1a, b, respectively.

Based on the numerical simulations, the computed water surfaces and velocity fields of the unsteady flood flow are shown in Fig. 2 at four different time instants, at $t = 1$, 2, 4, and 8 s, respectively. The simulations showed that the dam-break flows quickly propagated to the downstream region, and the flood route was altered due to the existence of the triangular barrier. This subsequently generated a large circulation zone arising from the flow–solid wall interactions. Here, the capability of the hybrid FEM–FVM model to reproduce complex flood flow patterns has been demonstrated.

To quantitatively validate the accuracy of numerical modeling, the computed time-dependent water surface levels at six measurement points (as shown in Fig. 1) are shown in Fig. 3 and compared with the experimental data of Brufau et al. (2004). The comparisons indicated that the general agreement is quite satisfactory, and the numerical model is able to predict the unsteady flood flow propagation and interaction with the triangular obstacle. Meanwhile, the location and amplitude of the shock waves are also well captured.

4.2 Dam-break flow over a mobile bed channel

In this section, we use the proposed hybrid FEM–FVM model to reproduce a laboratory experiment of mobile bed dam-break flow carried out in the Hydraulics Unit of the LEMSC, Catholic University of Louvain (Soares-Frazao et al. 2012). The computational domain is 27 m long, the width of upstream and downstream channels is 3.6 m, and a sluice gate is placed in the middle of the channel connection. The thickness of sediment layer is 0.085 m, which extends 1.5 m in the upstream side and 9.0 m in the downstream side. The mean diameter of sediment material is $d_{50} = 1.61$ mm, relative density

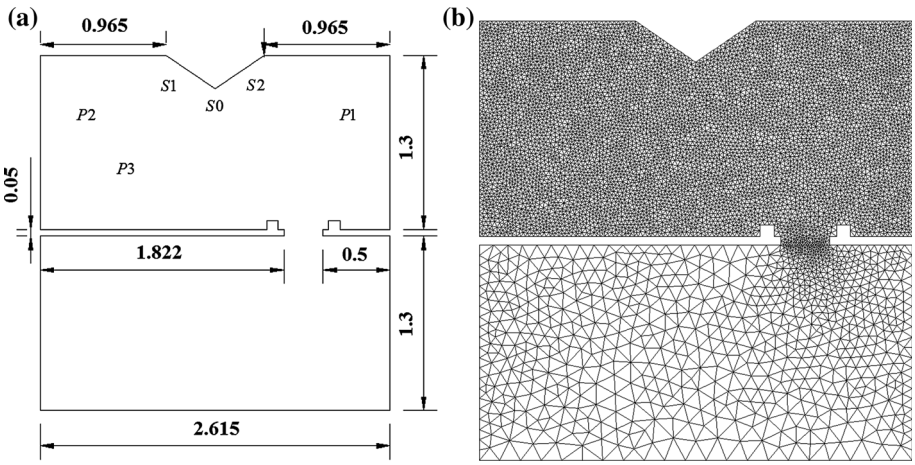

Fig. 1 Flood simulation in a horizontal 2D tank. **a** Domain layout and measurement points; **b** Computational meshes

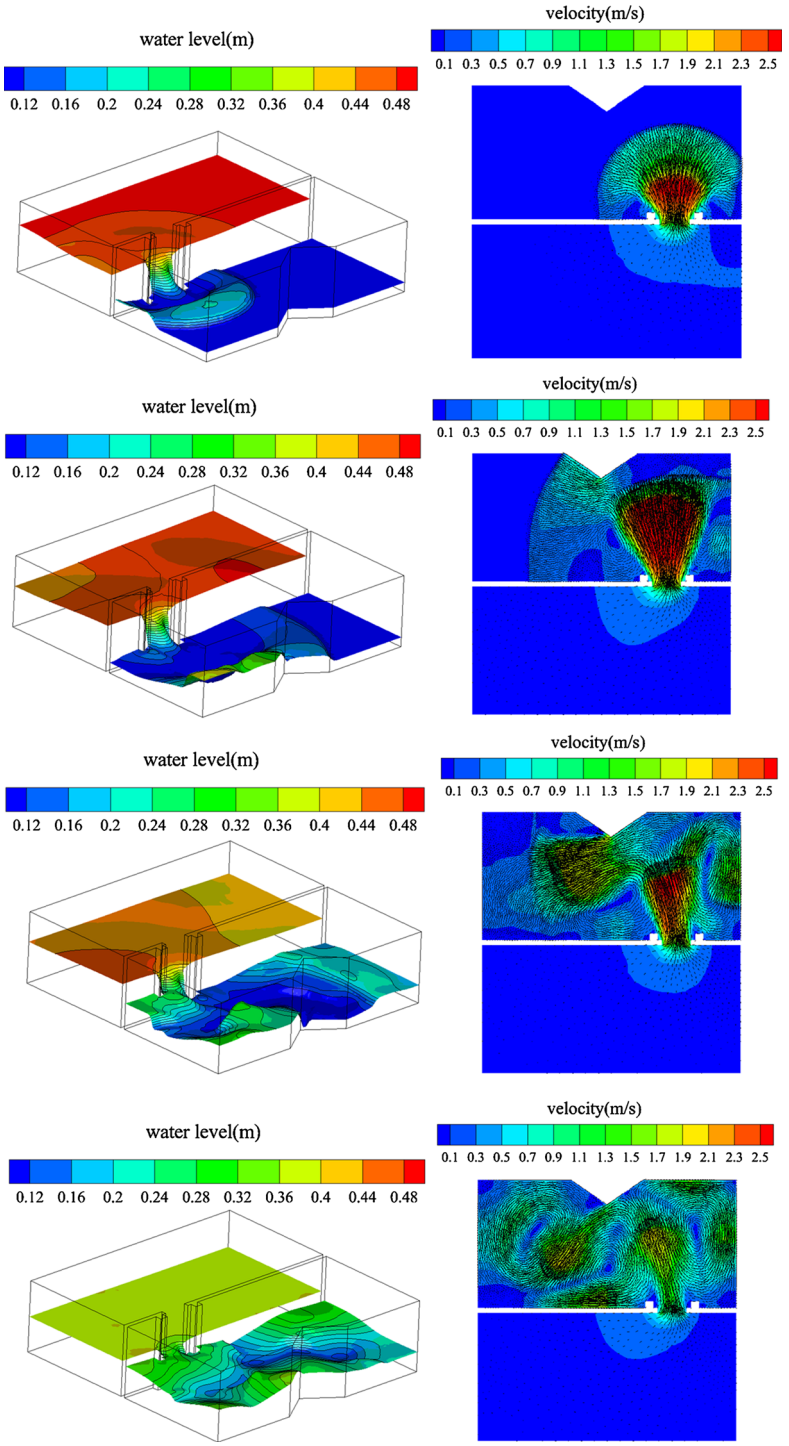
water level(m)
0.12 0.16 0.2 0.24 0.28 0.32 0.36 0.4 0.44 0.48
velocity(m/s)
0.1 0.3 0.5 0.7 0.9 1.1 1.3 1.5 1.7 1.9 2.1 2.3 2.5
water level(m)
0.12 0.16 0.2 0.24 0.28 0.32 0.36 0.4 0.44 0.48
velocity(m/s)
0.1 0.3 0.5 0.7 0.9 1.1 1.3 1.5 1.7 1.9 2.1 2.3 2.5
water level(m)
0.12 0.16 0.2 0.24 0.28 0.32 0.36 0.4 0.44 0.48
velocity(m/s)
0.1 0.3 0.5 0.7 0.9 1.1 1.3 1.5 1.7 1.9 2.1 2.3 2.5
water level(m)
0.12 0.16 0.2 0.24 0.28 0.32 0.36 0.4 0.44 0.48
velocity(m/s)
0.1 0.3 0.5 0.7 0.9 1.1 1.3 1.5 1.7 1.9 2.1 2.3 2.5

◀**Fig. 2** Computed water surface (*left column*) and velocity (*right column*) contours of flood flow in a horizontal 2D tank at $t = 1$, 2, 4, and 8 s (from *up* to *down*)

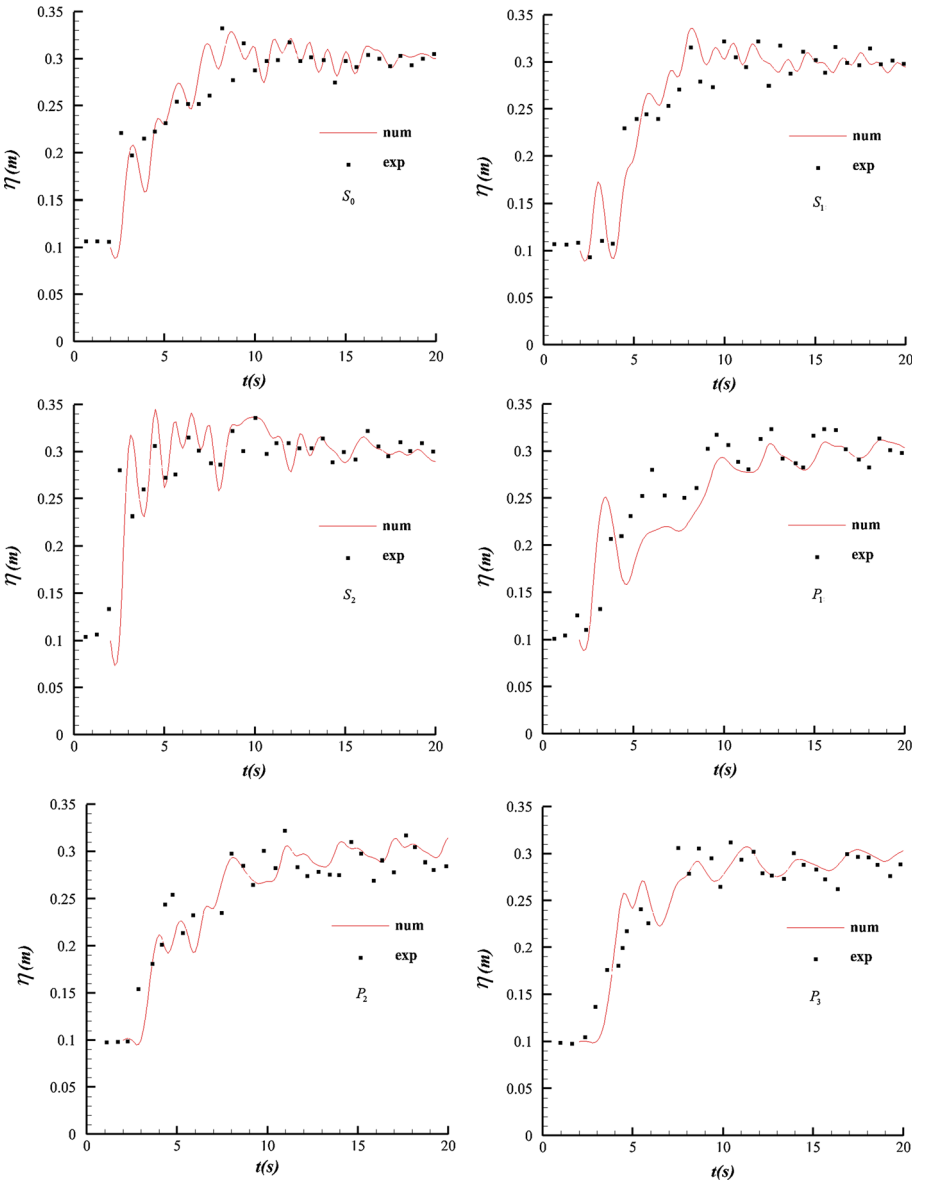

Fig. 3 Time history of computed (*lines*) and measured (*dots*) water surface levels of unsteady flood flow at measurement points $S_0, S_1, S_2, P_1, P_2, P_3$

$\rho_s/\rho_w = 2.63$, and bed porosity $\xi = 0.42$. The roughness is $n = 0.0165$ for the sediment bed and $n = 0.01$ for the fixed bed. The initial water depth in the upstream reservoir is 0.47 m, and the downstream channel is dry. The dam break was assumed to occur

instantly, and the subsequent flood process lasted for 20 s. A schematic setup of the computational domain is shown in Fig. 4a. To validate the numerical simulations, three measurement points and measurement profiles in the longitudinal direction of the channel are taken in the computational domain as shown in Fig. 4b.

The computed water surface levels and sediment bed deformations are shown in Fig. 5, and the velocity fields and flow Fr numbers are shown in Fig. 6, respectively, at three selected times at $t = 2.0$, 8.0, and 20.0 s, respectively. The erosion and deposition results in Fig. 5 indicated that as the dam-break flow propagated over the mobile bed, it caused severe erosion at the original dam site. Later on, with the change in local flow and bed conditions, the dam-break flow reduced its capacity and deposited the sediment materials in the downstream area, forming something like an alluvial fan. Besides, the water surface contours showed the generation and evolution of strong dam-break shock waves propagating in the downstream direction, which led to irregular wavy water surfaces. Generally speaking, the dam-break flow could generate significant sediment erosions and depositions in a very short period of time and thus constitute a rapid alluvial process. For example, the sediment bed layer at the dam site was nearly eradicated at time $t = 8$ s after the dam break, and the maximum deposition height added up to 7 cm around $t = 20$ s. As

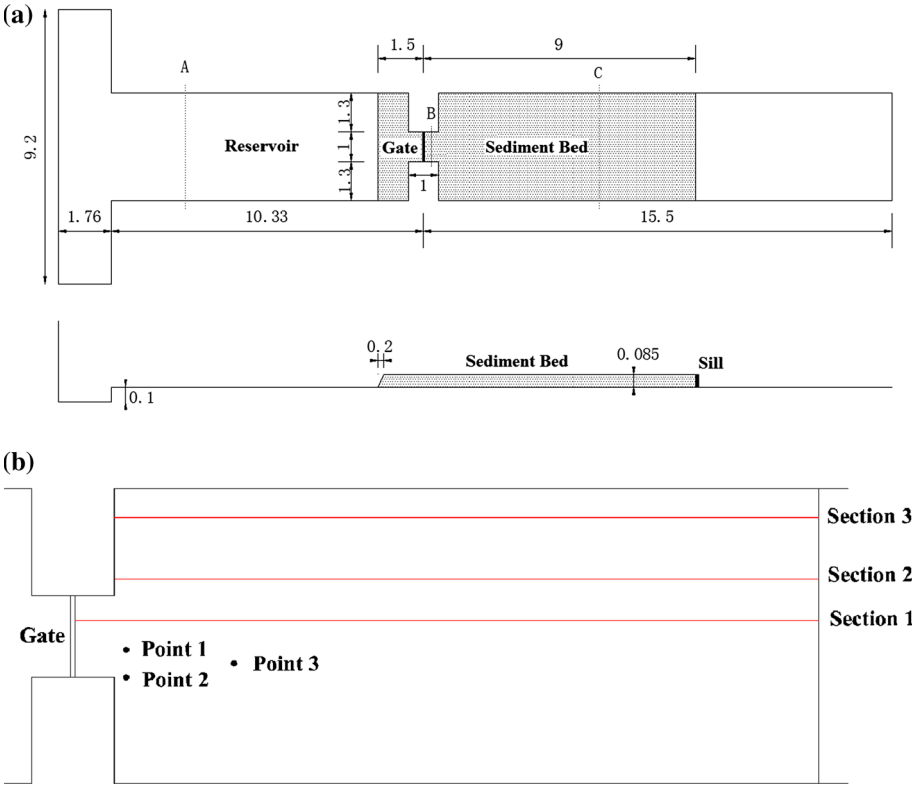

Fig. 4 **a** Schematic setup of computational domain for mobile bed dam-break flow (unit in meter); **b** Locations of measuring points and profiles

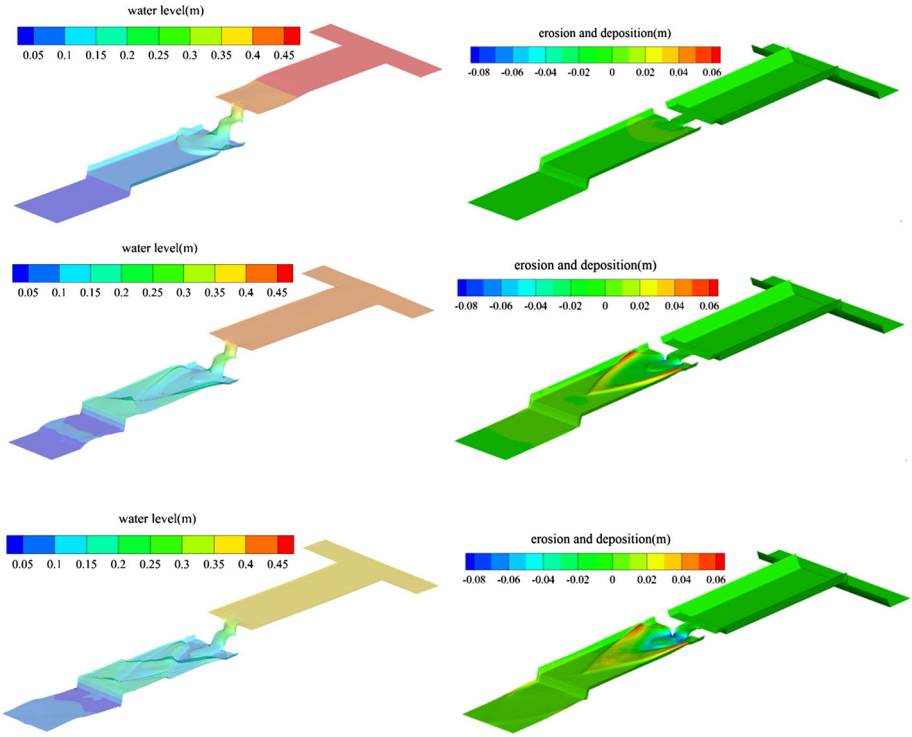

Fig. 5 Computed water surface (*left column*) and sediment bed deformation (*right column*) contours of mobile bed dam-break flow at $t = 2$, 8, and 20 s (from *up* to *down*)

a result, a total of around 14-cm topographic difference in the original flat bed was generated within a short timescale.

The velocity fields in Fig. 6 show that in the early stage of dam break, the high-velocity area concentrates near the dam site, but it spreads out along the centerline of the channel as time goes on and the flow intensity also tends to decrease. The mobile sediment layer has an obvious effect on the dam-break process and acts as a buffer zone to reduce the flow velocity, which is demonstrated by the fact that the velocity in the fixed bed portion of the channel as shown at time $t = 8$ s is larger than that in the sediment channel in the cross-sectional area. Besides, the Froude number contours have also showed a similar trend. Although the flow regime is supercritical in most of the downstream areas, the flow intensity becomes smaller and more uniformly distributed at the later stage of dam-break process.

The comparisons between the simulated and measured water surfaces as well as sediment bed elevations are shown in Fig. 7. Generally speaking, the agreement between the numerical simulations and experimental measurements is quite satisfactory in the engineering interest by considering the complex water–sediment interactions and efficient simulation time of the model using a hybrid FEM–FVM solution scheme. However, relatively larger errors can be found for the measuring point 3 and Sect. 1, which is due to the correlation of computational errors between the water surface level and bed deformation.

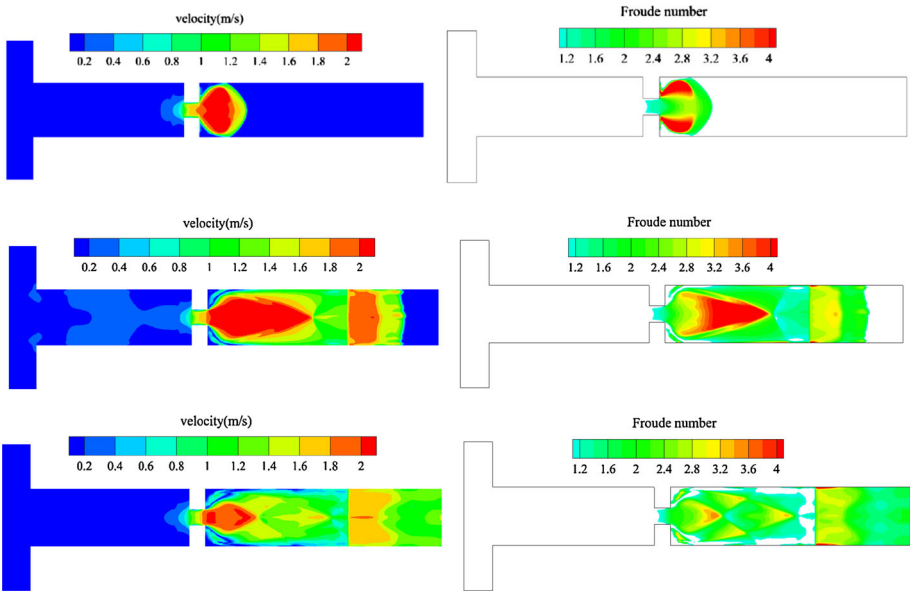

Fig. 6 Computed flow velocity (*left column*) and Fr number (*right column*) contours of mobile bed dam-break flow at $t = 2$, 8, and 20 s (from *up* to *down*)

4.3 Morphological modeling of dam removal experiment

To validate the numerical model in the prediction of morphological changes at the dam site area, the benchmark laboratory experiment of Cantelli et al. (2004) is used. The original work reported on the erosion of a deltaic front induced by the removal of a dam. The installation of a dam on the river induces sedimentation at the upstream end of the reservoir. The removal of a dam causes erosion into the resulting deposit and subsequent disastrous sediment flows. Not many numerical models have been developed to model such a complex process including the erosion, transport, and deposition of sediment due to the difficulties in treating the steep streamwise bed slope created by the dam removal that induces high flow velocities and sediment transport rates, and the variations in the width of the channel incising into the deposit.

According to Cantelli et al. (2004), the experiments were performed at St. Anthony Falls Laboratory, University of Minnesota. A rectangular glass-walled flume 14 m long, 0.61 m wide, and 0.48 m high was modified to model a long reservoir of uniform width. The initial slope of the sediment bed was 1.8 %. The dam was located 9 m from the inlet of the flume. To simplify the problem, non-cohesive sediment was used in the experiment. Ten runs using different water flow discharges and dam removal procedures were considered in the experiment, and we reproduce Run 6, which is an instantaneous collapse.

The model simulation time duration is 5600 s, which is set to be consistent with the physical experiment (Cantelli et al. 2004). The numerical domain is 14 m long and 0.61 m wide. Non-structured grids were used with 29,518 nodes and 57,570 grids. The roughness of the channel bed was taken as 0.016. Computational time step was automatically adjusted

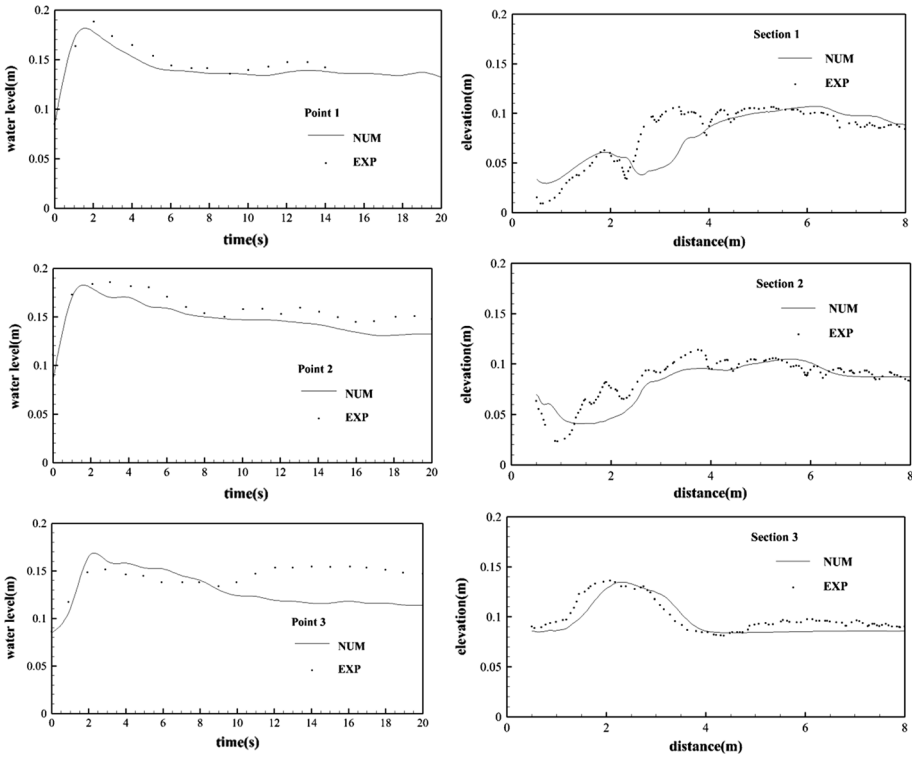

Fig. 7 Measured and computed water surface levels (*left column*) and sediment bed elevations (*right column*)

based on a CFL condition of 0.4. The flow discharge rate is $Q = 0.3 \times 10^{-3}$ m^3/s, and the sediment grain size is $D_{50} = 0.8$ mm.

Figure 8 shows the evolutions of the bed profiles along the channel center during the erosion of the reservoir deposits at different time instants. The erosion upstream of the deposit front and the deposition downstream is clearly visible. The dotted line in the figure represents the initial bed profile. It shows that after the sudden removal of the dam, the flow incises into the reservoir deposit, first rapidly and then more slowly. Toward the end of model simulation around time $t = 5600$ s, the equilibrium bed slope is approximately equal to the initial slope value. A very good agreement in the morphological profiles has been found between the numerical simulations and measurement data of Cantelli et al. (2004) in Fig. 8. Slightly large discrepancies only appear at $t = 5600$ s near the far downstream side of the deposit, which is probably due to the numerical parameter uncertainties after the long-time simulation.

Furthermore, the computed 3D longitudinal channel profiles are shown in Fig. 9, for the time instants at $t = 1$ min and 1.5 h, respectively, after the erosion started. It clearly demonstrated the spatial and temporal variations in the incision and widening of the channel. The so-called erosional narrowing as found by Cantelli et al. (2004) in their laboratory experiment was also found in the present numerical simulations.

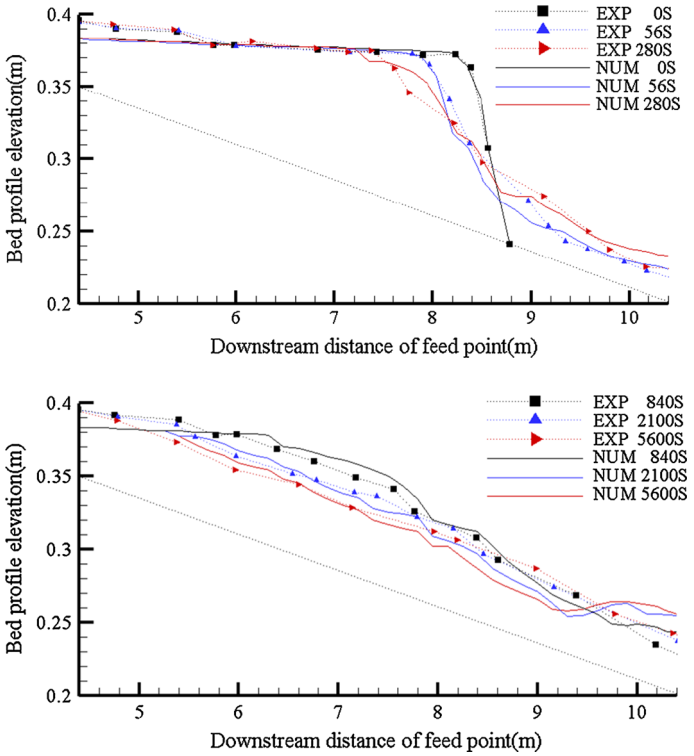

Fig. 8 Computed and measured time evolution of bed profiles along the channel center (dam located 9 m downstream of the feed point and flow from *left* to *right*, following Cantelli et al. 2004)

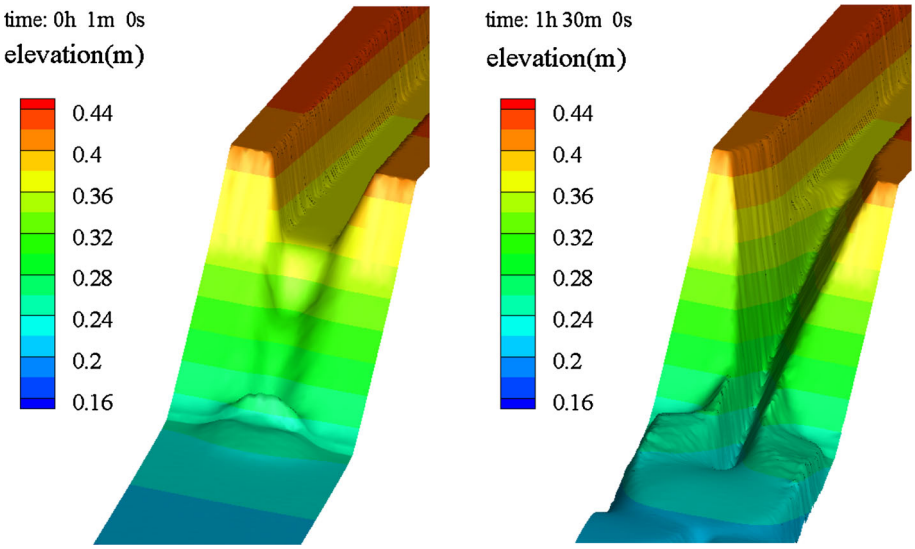

Fig. 9 Three-dimensional longitudinal profiles of channel erosion process

5 Model applications in field case study

5.1 Sediment-laden flood flow at Polo Hydropower Plant

The Polo Hydropower Plant is located at the two river confluence in the Yi Autonomous Region of Sichuan Province, which was put into operation in December 1999. During the heavy rainstorms of July 28, 2001, the sediment-laden floods from the two rivers inundated the power plant. The situation was further deteriorated by the large quantities of sediment deposition, which raised the riverbed by about 5–7 m. The two rivers near the confluence region demonstrated mountainous river features with relatively steep bed slope. The flow regime was quite complicated due to the drastic changes in topographic and boundary conditions. To reinvestigate this natural disaster and provide useful information for the engineering practice in future, in this study we carry out both the physical experiment and numerical simulation to reproduce the flood and sediment transport process near the river confluence. The physical experiment was carried out at the State Key Laboratory of Hydraulics and Mountain River Engineering, Sichuan University.

The topographic data of the site were obtained from the field survey carried out 2 years before the 2001 sediment-laden flood disaster. The field photograph of the original Polo Hydropower Plant and a schematic layout of the nearby rivers are shown in Fig. 10a, b, respectively. The detailed river systems are introduced as follows: The upstream flow inlet of one tributary river, which is called the Wahei River, is 250 m away from the confluence junction. The upstream inlet of another tributary river, called the Xianjiapu River, is 200 m away. The downstream flow outlet is 150 m away from the confluence point. For a comparison, the field photographs of the hydropower plant after being damaged by the flood and sediment flows in July 2001 are shown in Fig. 11a, b.

5.1.1 Modeling parameters

The detailed modeling conditions are taken as follows. Due to the lack of real-time observations of flow and sediment hydrographs during the flood event, here we simply use the peak flow discharges of the July 28 flood as input parameters for the present physical and numerical models. That is to say, we assume the Wahei River has a flow discharge of 1350 m^3/s ($P = 2$ %), and Xianjiapu River has a flow discharge of 712 m^3/s ($P = 5$ %).

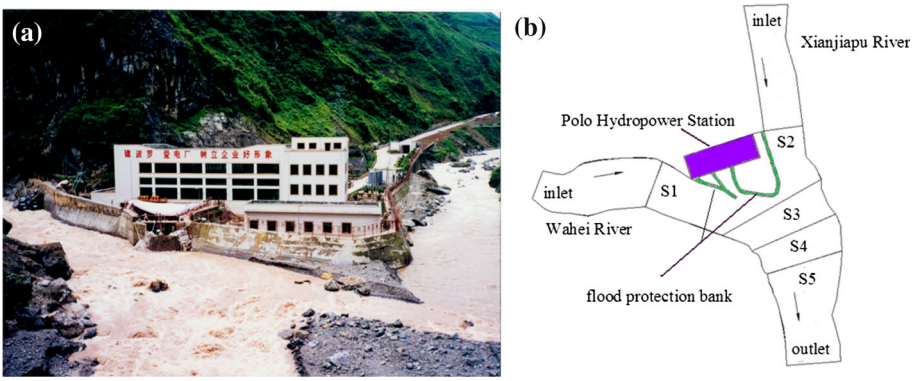

Fig. 10 **a** Field photograph of original Polo Hydropower Plant; **b** schematic layout of rivers

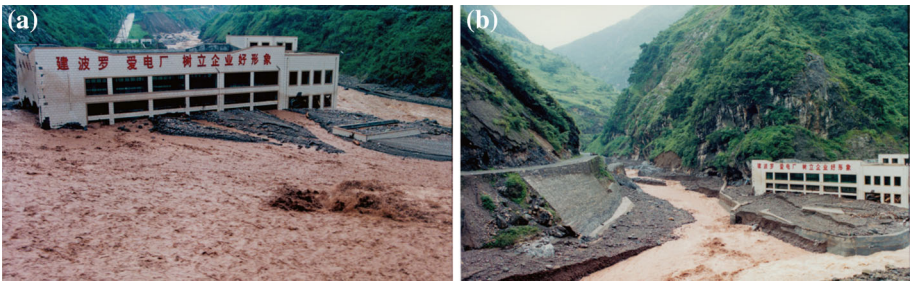

Fig. 11 Field photograph of damaged Polo Hydropower Plant caused by **a** flood flows; **b** sediment deposits

The sediment concentration is assumed to be in saturation at the upstream river inlets, and the free outflow boundary conditions are imposed at the downstream flow outlet. The gradation of the sediment materials is shown in Table 1.

5.1.2 Flood flow simulation results and analysis

In the first phase of the study, we carried out physical experiment and numerical simulations for the water flow only without considering the sediment transport. Figure 12a, b shows the inundation of the hydropower plant due to the confluence of floodwater from the two river tributaries. The physical experimental photograph in Fig. 12a and the numerical water level in Fig. 12b are qualitatively compared together, and it shows that the two converging rivers caused significant flooding damages to the hydropower plant.

To further investigate the flood flow features, the water surface profiles at two measurement sections S1 and S2 (as shown in Fig. 10b) are compared between the numerical results and experimental data in Fig. 13a, b, respectively. Besides, the computed flow velocity field and its good agreement with the experimental measurement are shown in Fig. 14a, b.

It can be seen from Figs. 13 and 14 that the inundation of the hydropower plant was caused by two different flood scenarios: (1) As the tributary river—Wahei River—has relatively steep bed slope, irregular channel cross section, and meandering flow pattern, the direct flow thrust and deflection of this river caused the floodwater to overtop over the protection bank. This can be easily understood through Fig. 13a for the cross-sectional water level at Section S1, where there exists a large difference in the water surface levels of about 7.45 m. (2) On the other hand, another tributary river—Xianjiapu River—inundated the hydropower plant due to the floodwater from the two tributary rivers running against each other. The interaction of the two rivers reduced the local flow velocity and accordingly increased the flow depth, resulting in the water level being higher than the protection bank. This can be partly demonstrated by the cross-sectional water level in Fig. 13b at measuring section S2, as well as the flow velocity field near the confluence area in Fig. 14.

Table 1 Gradation of sediment materials at upstream inlet

Diameter (mm)	>500	500–200	200–60	60–20	20–5	5–2	2–0.5	0.5–0.25	<0.25
Percentage (%)	0.0	28.8	10.5	18.7	16.8	17.3	6.1	1.0	0.8

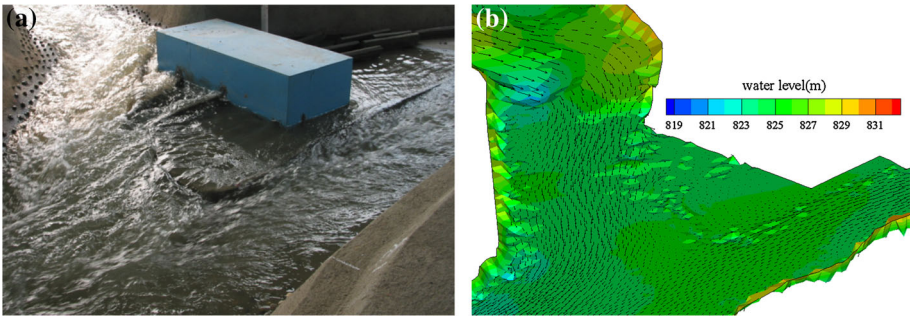

Fig. 12 Flood inundation of the hydropower plant due to river confluence. **a** Physical experiment; **b** numerical simulation

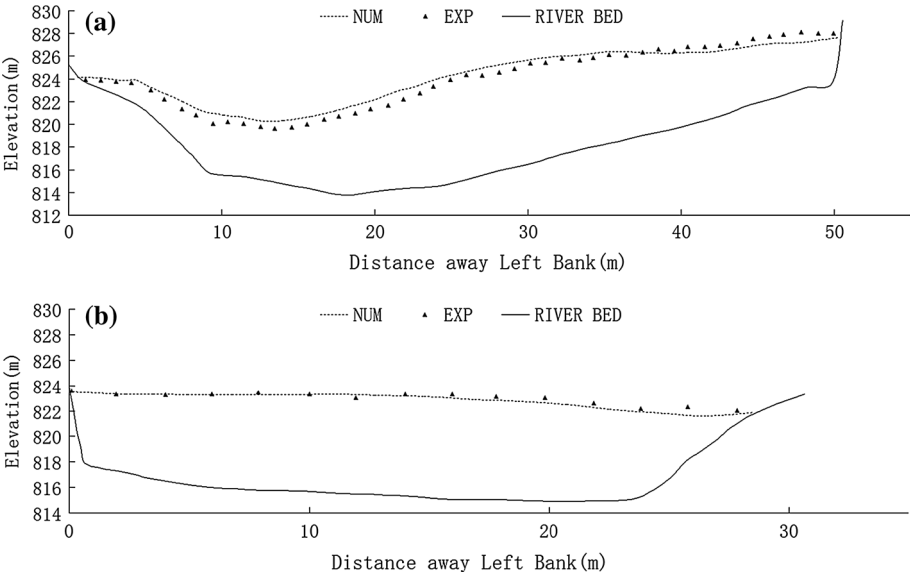

Fig. 13 Computed and measured water surface profiles in cross-sectional area at measurement sections **a** S1; **b** S2

Besides, in both Figs. 13 and 14, the numerical results agree quite well with the experimental data, indicating the accuracy of the proposed FEM–FVM model in water flow simulations.

5.1.3 Sediment simulation results and analysis

In the second phase of the study, the physical experiment and numerical simulations for the mobile bed condition were carried out, based on the previous fixed bed works by feeding the sediment materials into the river system at the upstream flow inlets. The aim was to investigate the sediment transport and deposition process near the river confluence and evaluate its influence on the inundation of the Polo Hydropower Plant. An illustrative

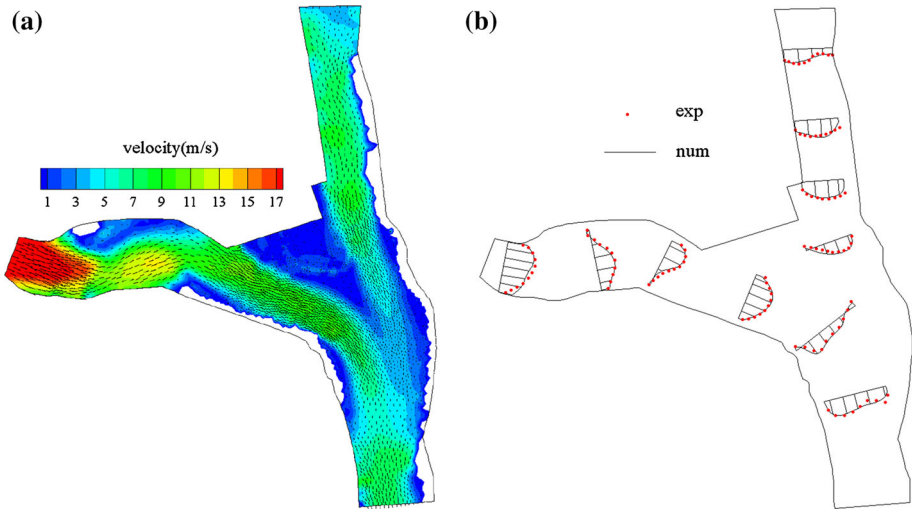

Fig. 14 **a** Computed velocity field; **b** comparisons of experimental and numerical velocities near the river confluence area

Fig. 15 Experimental photograph of sediment deposition near the hydropower plant

photograph of the experimental site is shown in Fig. 15, which shows that the sediment deposition near the river confluence also contributed to the damage of the power plant.

Figure 16 shows the sediment deposition thickness and water-level contours at time $t = 1$, 2, 4, and 6 h of the numerical simulations. The left column is the deposition layer thickness, and the right one is the water level. Figure 16 demonstrates the importance of river confluence on the sediment transport and deposition features, which contributed to the raising of riverbed and deteriorated the flood disasters. Due to the blocking effect of the Wahei River along the Xianjiapu River's flow route, the sediment-laden capacity of the latter was greatly reduced, leading to severe sedimentation of the riverbed. On the other hand, due to that the upstream sediment input of the Wahei River was very rich and the existing river training works blocked part of the flow channel, the water surface slope in the confluence area was much smaller as compared with its upstream value. This situation was made more serious by the two river interactions, i.e., one river flowing against another as mentioned before. As a result, some large sediment materials such as gravels were first deposited in the confluence region. However, this deteriorated the situation by further

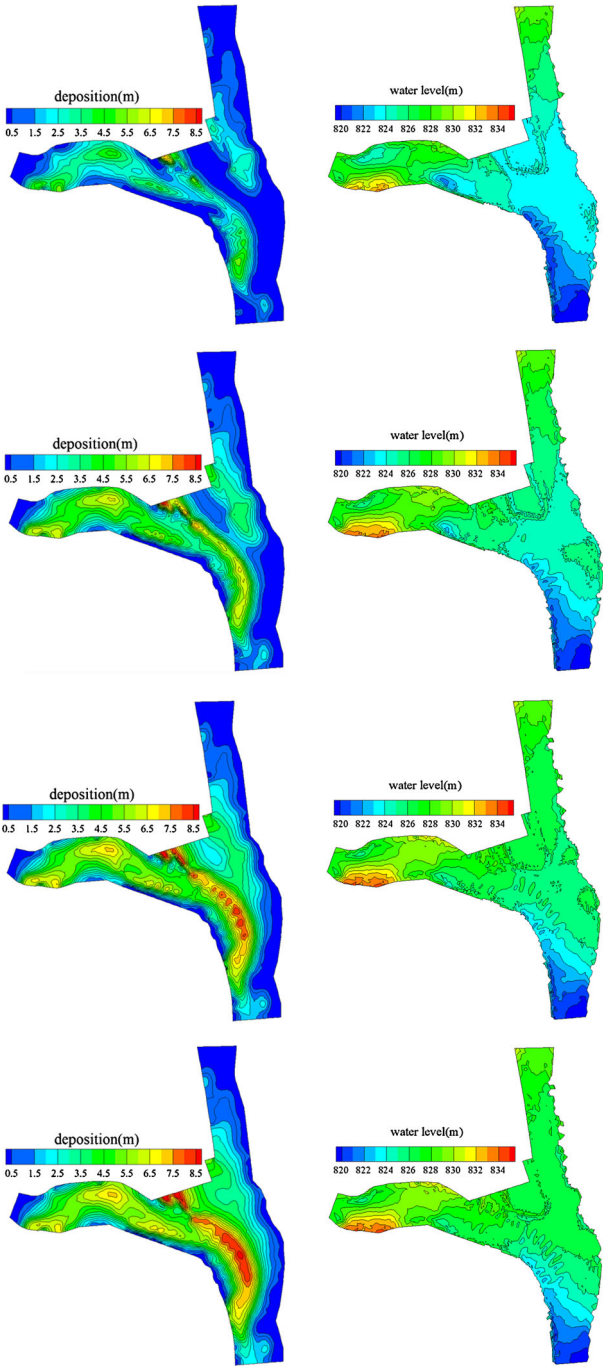

Fig. 16 Computed sediment deposition thickness (*left column*) and water surface level (*right column*) contours near river confluence at $t = 1$, 2, 4, and 6 h (from *up* to *down*)

reducing the local water surface slope and caused more medium and even small sediment materials to be settled. Finally, the thickness of the sediment deposits gradually exceeded the height limit of the river protection bank, and large quantities of the sediment materials were dumped into the hydropower plant.

To quantitatively validate the accuracy of the numerical model for long-time flow and sediment simulations, Fig. 17a–c shows the computed and measured sediment bed profiles for the measurement Sections S3–S5 as shown in Fig. 10b. In spite of some discrepancies in the data set due to the complexity of the problem, the two results agree quite well in view of the engineering interest, and it shows the numerical simulations realistically reproduced the sediment transport and deposition process during the two river confluence. According to the field observation records, large-scale landslides also happened during the storm flood, and thus, plenty of the debris stones were dumped into the power plant, with some gravel stones having diameter as large as 1.0 m. They have generated catastrophic effect on the damage of the building, but they were difficult to model in either the physical experiment or numerical simulations.

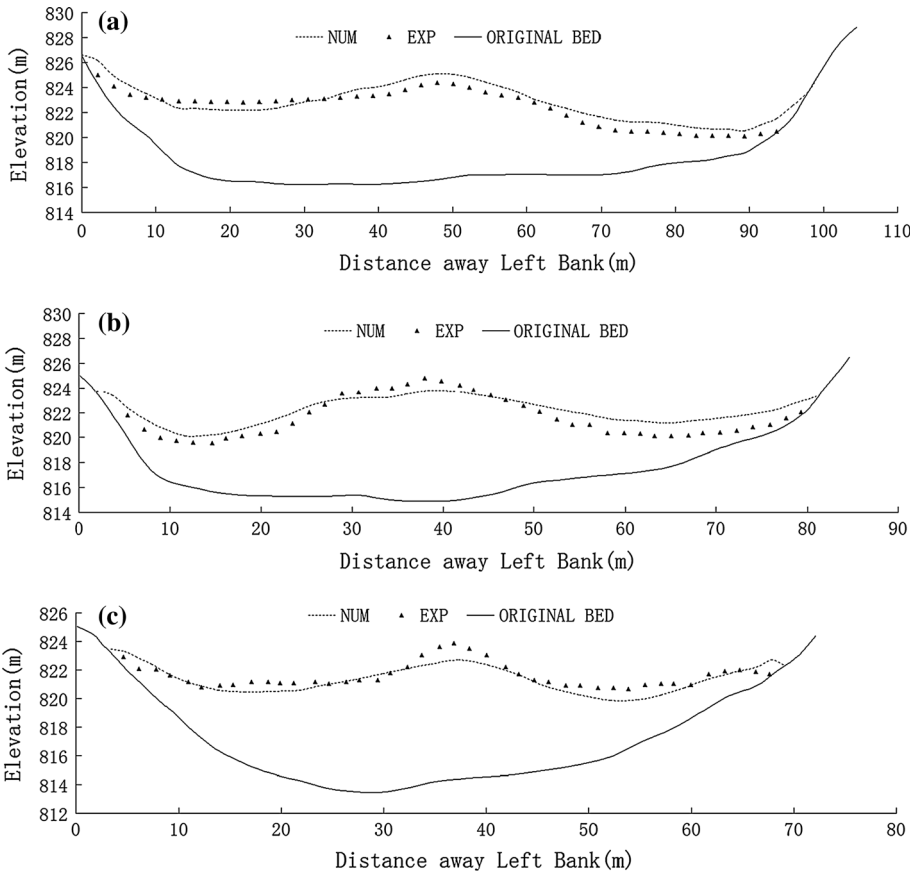

Fig. 17 Computed and measured sediment bed profiles in cross-sectional area at measuring sections **a** S3; **b** S4; **c** S5

The disagreement between the physical experiment and numerical simulations could be attributed to several reasons. Firstly, the simulation of mountainous rivers over relatively steep bed slope requires more stable numerical schemes, and some numerical treatments adopted in this paper could bring uncertainties and affect the simulation accuracy. Secondly, the present river systems have a bed slope around 0.04, and the characteristic sediment diameter is 35 mm, while the Meyer–Peter formula used in the FEM–FVM model only applies to the bed slope being less than 0.02 and sediment diameter being in the range of 0.4–29 mm. Lastly, the proposed numerical model uses the averaged horizontal velocities to compute the bed load transport. This approach did not adequately address the influence of secondary flows which are quite important in mountainous rivers.

5.2 Tangjiashan mountain 2013 flood

5.2.1 Engineering background

Tangjiashan Mountain Lake was formed during the Wenchuan Earthquake that happened in May 12, 2008, and it is located 5 km upstream of the Old Town of Beichuan. The length of the dam is 803 m along the river flow, and the maximum cross-sectional width is 611 m. Due to the adequate engineering works carried out after the Wenchuan Earthquake, the water level in the lake reservoir has been maintained at a safety level of 713 m, and the water storage capacity is around 86 million m^3. On July 9, 2013, the heavy precipitations in the catchment area reached as large as 285 mm, which raised the water level of the Tangjiashan Lake by 8.0 m. As a result, the right portion of the dam was partially breached leading to a flood with maximum discharge rate of 5000 m^3/s. Subsequently, quite a few downstream areas were inundated with the submergence depth exceeding 7.0 m. The damaged areas include some heritage sites such as the Beichuan Hotel and Cemetery of Victims. Figure 18 shows the site photograph of the flood and post-flood sediment inundation areas near Beichuan Hotel.

5.2.2 Computational domain and model parameters

The whole computational domain includes the Tangjiashan Lake in the most upstream area and 1.85 km downstream of the Old Town of Beichuan, with a total length of 8.6 km. The plan view and topographic contours of the computational area are shown in Fig. 19a, b. According to the field survey, the river channel upstream of the Beichuan Hotel has a bed

Fig. 18 Site photograph of flood and post-flood sediment (circled in *red line*) inundations near Beichuan Hotel (http://www.chinanews.com/shipin/2013/07-12/news251654.shtml)

roughness of $n = 0.042$, and the downstream area from this location has $n = 0.04$. The numerical simulations aim to reproduce the flooding and sediment process for the next 7 days after the dam-break flow disaster. For the boundary conditions, the upstream inflow hydrograph and downstream rating curve are shown in Fig. 20a, b, respectively.

At the beginning of the computation, the river channel is treated as being dry. As described by Chen et al. (2011), in order to obtain a good-shaped wet–dry boundary line, a minimum threshold water depth h_{min} is used. A node is regarded as being dry when its water depth is less than h_{min}; otherwise, it is marked as being wet. A grid including any dry node is treated as a dry grid unless it contains all of the wet nodes, in which case it is regarded as being wet. The upstream sediment input is assumed to be from the breached dam materials rather than from the Tangjiashan Lake area. The bed materials of the channel are composed of three layers, and the sediment size gradations for each layer are shown in Table 2 as below.

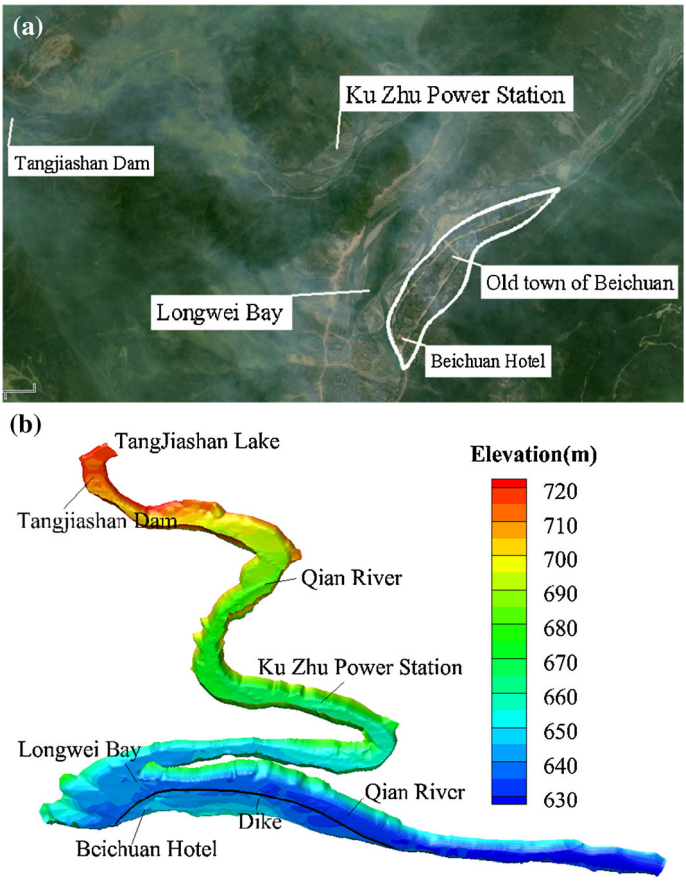

Fig. 19 **a** Plan view (from google map); **b** topographic contours of computational domain, including key control locations

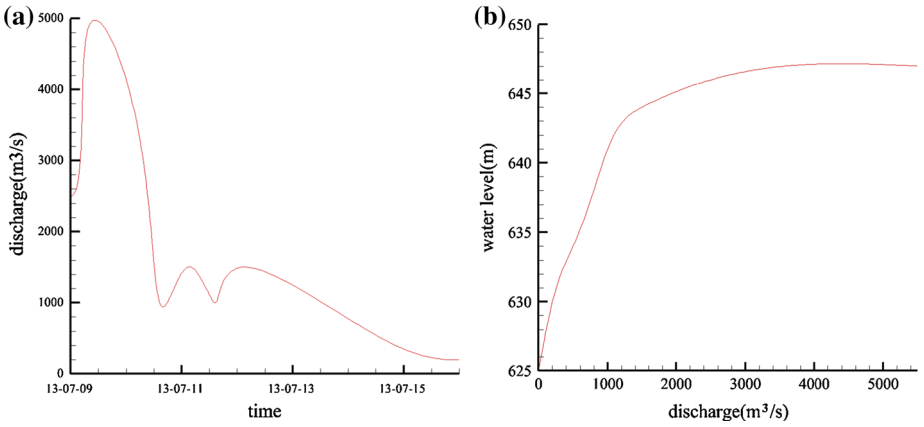

Fig. 20 **a** Upstream hydrograph; **b** downstream rating curve for model input

Table 2 Sediment layer thickness and grain size gradation of each layer

Sediment layer thickness (m)	Gradation of sediment grain size in percentage (%)					
Sediment size (mm)	200–60	60–20	20–5	5–2	0.5–0.25	<0.25
2 (upper layer)	37.2	27.8	16.3	6.6	6.7	3.4
2 (middle layer)	24.8	24.5	18.3	12.1	15.5	4.8
5 (lower layer)	48.2	14.6	8.2	10.2	14.4	4.4

5.2.3 Modeling results and discussions

Figure 21 shows the computed velocity fields after the dam-break flood at time $t = 1$, 2, 6, 24 h, 3, and 7 d, respectively. It shows that the flooding water propagates about 2.9 km downstream of the dam at $t = 1$ h. The flow velocities decrease from the dam site, which are around 5.0 m/s, to about 1.0 m/s toward the downstream region due to the widening of the channel and the flow energy dissipation from bed friction. At $t = 2$ h, the flood flow reaches the downstream of Longwei Bay with a smaller front velocity of 1.2 m/s as a result of the spacious flow path. It has been observed in the model simulation that the flow arrives at the outlet boundary of the model at time $t = 2.7$ h. Due to the continuous supply of flooding water from the dam reservoir, the general velocity amplitude increases at $t = 6$ h, which is demonstrated by the fact that the main flow velocity upstream of the Longwei Bay exceeds 5–10 m/s, while the corresponding downstream velocity is also as high as 3–5 m/s. After $t = 24$ h of the dam break, due to the reduction in the upstream flood input, the general flow velocities tend to decrease. However, due to the erosion of the upstream main channel, the converged water still maintains sufficient momentum. Between $t = 3$ and 7 d, the flow velocities start to demonstrate a decreasing trend, due to the continuous reduction in the upstream water supply. Finally, all of the flooding water returns to the main channel, and there exists a clear difference in the flow patterns at upstream and downstream of the Longwei Bay.

The sediment erosion and deposition of the riverbed are shown in Fig. 22 for the next 3 days after the dam-break flood. It is shown that by one day later, most of the alluvial

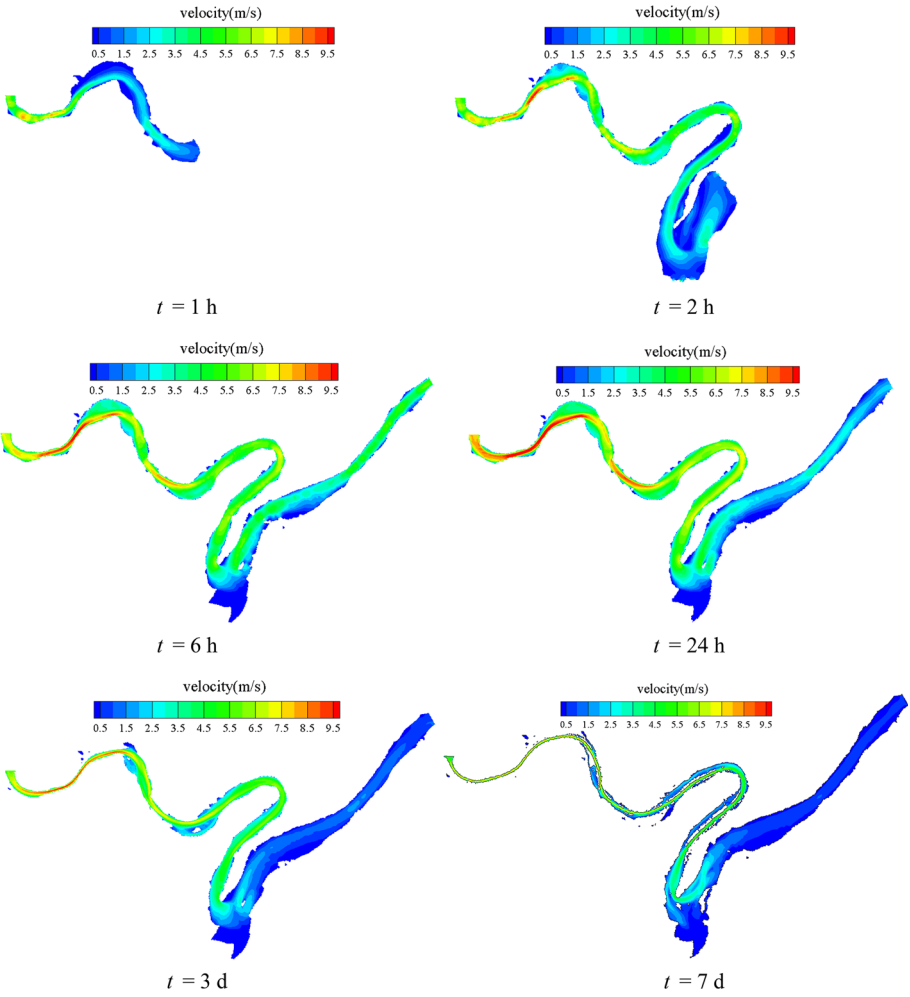

Fig. 21 Computed velocity fields of flood flow at different times

processes happen near the dam area. This is demonstrated by the fact that severe erosions are found immediately downstream of the Tangjiashan Dam, and further downstream channels show the features of erosion in the main channel and deposition on the side bank. Then, 3 days later, the erosion of the main channel has progressed to somewhere upstream of the Longwei Bay. Finally, 7 days after the dam break, a quasi-equilibrium state of the alluvial evolution has achieved, demonstrated by the clear erosion of the main channel which deposited the sediment materials onto the side bank. The deposition thickness near the Longwei Bay reaches as high as 5–10 m.

To validate the model simulations, the alluvial pattern of the bed on 7th day is compared with the field observations in Fig. 23, and the computed flow inundation depth near the Beichuan Hotel is shown in Fig. 24 (for the enlarged area as indicated by the square in Fig. 22c). The comparisons in Fig. 23 show a similar deposition pattern near the Longwei Bay between the numerical results and field observations. The differences lie in that the measured thickness of the deposit is higher than that from the numerical simulations by

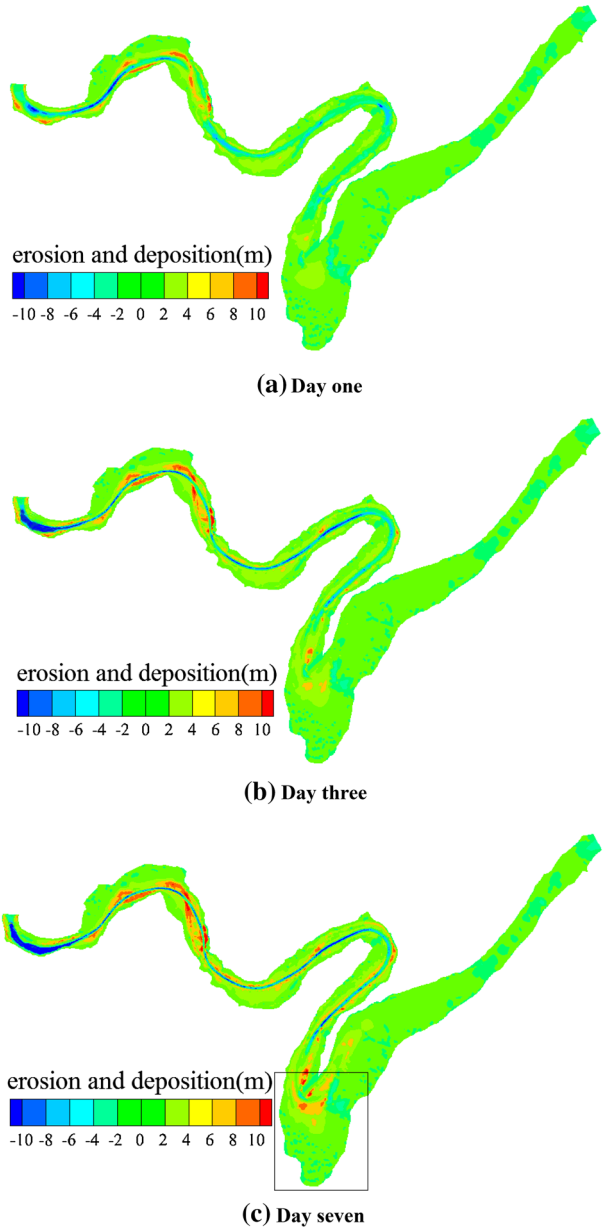

Fig. 22 Alluvial process of dam-break flood in downstream areas

about 2.0 m near the front of the alluvial fan. Besides, the discrepancy also appears in the deposition area of the main channel and side bank. This could be due to that, in the numerical model, the sediment movement is controlled by the flow velocity field, and the smaller velocity calculated on the side bank cannot transport much sediment material. However, in practice, some hyper-concentrated flows in the form of slurry have been found on the surface of the deposits which continued to move downstream to reshape the alluvial

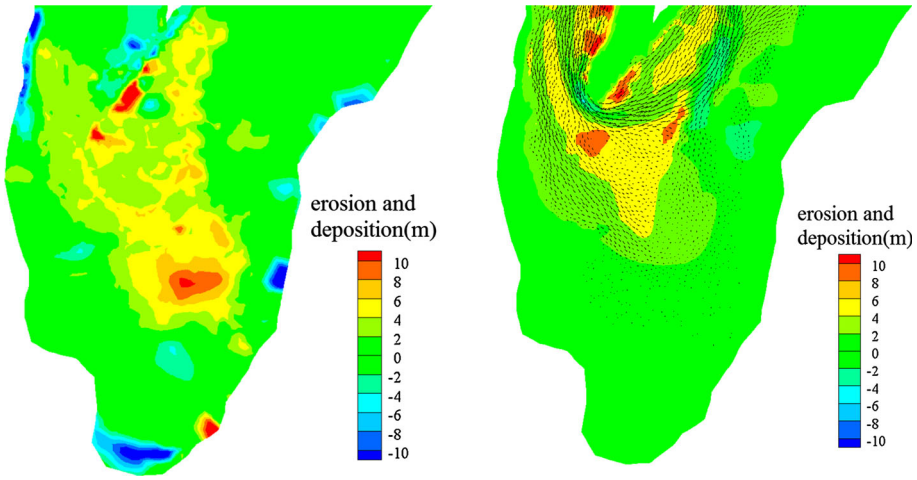

Fig. 23 Alluvial pattern of bed 7 days after the dam-break flood (*left* field observation; *right* numerical result)

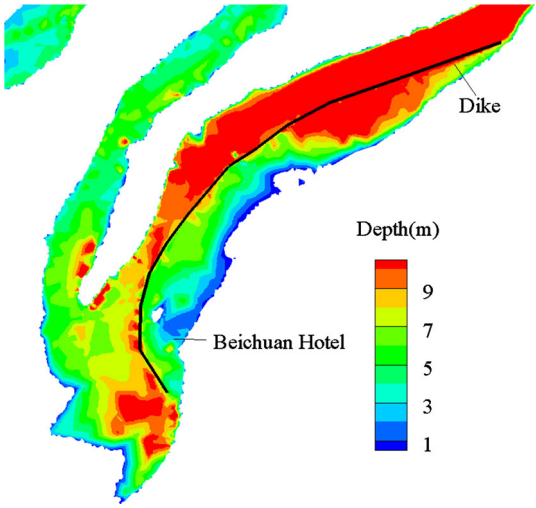

Fig. 24 Computed flow inundation depths near Beichuan Hotel and Dike area

process. Furthermore, the simplifications of initial and boundary conditions in the numerical model could also cause uncertainty in the result predictions. In addition, the inundation depths computed in Fig. 24 indicate that most of the areas near the Beichuan Hotel and Dike have been flooded by the water up to more than 8.0 m. This is also quite consistent with the field observations and the media report.

6 Conclusions

The paper combined the FEM characteristic splitting method and FVM Godunov scheme and developed a water–sediment mixture flow model for the field river studies in Southwest China. The FEM numerical algorithm is robust for the treatment of advection term

and flexible in fitting the complicated physical boundary, while the FVM solution scheme has satisfactory conservation property and numerical accuracy. Through a series of benchmark unsteady flow tests and two field case applications, the hybrid FEM–FVM model has been found to have good stability and accuracy when the numerical results were compared with the experimental data. The study demonstrates that the present numerical model could provide a simple and useful prediction tool for the water–sediment mixture flow problems in engineering field as an economic substitute for the physical experiment and field observation.

In order to more accurately forecast the practical sediment transport and alluvial deformation, more sound sediment erosion and deposition mechanisms should be explored in the future work. As fundamental sediment properties could behave significantly different from one region to another (Wang and Zhang 2012), further investigations on the sediment initiation, sediment-laden capacity, sediment settling velocity, etc., should be of more priority than the development of higher-order numerical schemes. This is especially true shall the model be applied to the practical field cases in different regional areas.

Finally, we would like to mention that the main objective of the present research is to use the numerical model to evaluate the dam-break flood in the downstream areas. However, in many engineering situations, the upstream flow structures and sediment erosion and sedimentation properties, such as the dam failure hydrograph and morphological changes at the dam site, are of particular interest in the engineering community as documented by Wang et al. (2008) and Liu et al. (2012a, b). Also, these could provide a more robust test on the capacity of the numerical models.

Acknowledgments This research work is supported by the Start-up Grant for the Young Teachers of Sichuan University (No. 2014SCU11056), National Science and Technology Support Plan (No. 2012BAB0513B0), and Open Fund of the State Key Laboratory of Hydraulics and Mountain River Engineering, Sichuan University (No. SKHL1409). Finally, we kindly acknowledge the constructive discussions with Dr Jaan Hui Pu at Bradford University, UK, during the manuscript preparations.

References

Brufau P, Garcia-Navarro P, Vazquez-Cendon ME (2004) Zero mass error using unsteady wetting-drying conditions in shallow flows over dry irregular topography. Int J Numer Meth Fluids 45(10):1047–1082

Cantelli A, Paola C, Parker G (2004) Experiments on upstream-migrating erosional narrowing and widening of an incisional channel caused by dam removal. Water Resour Res 40:W03304. doi:10.1029/2003WR002940

Cao ZX, Yue ZY, Pender G (2011) Landslide dam failure and flood hydraulics. Part II: coupled mathematical modelling. Nat Hazards 59:1021–1045

Casulli V, Zanolli P (2002) Semi-implicit numerical modeling of nonhydrostatic free surface flows for environmental problems. Math Comput Model 36:1131–1149

Chen RD, Liu XN, Cao SY, Guo ZX (2011) Numerical simulation of deposit in confluence zone of debris flow and mainstream. Sci China Technol Sci 54(10):2618–2628

Demirbilek Z, Nwogu OG (2007) Boussinesq modeling of wave propagation and runup over fringing coral reefs, Model Evaluation Report, Technical Rep. No. ERDC/CHL TR-07-12, U.S. Army Corps of Engineers, Vicksburg, MS

Du CJ (2000) An element-free Galerkin method for simulation of stationary two-dimensional shallow water flows in rivers. Comput Methods Appl Mech Eng 182:89–107

Guillou S, Nguyen KD (1999) An improved technique for solving two-dimensional shallow water problems. Int J Numer Meth Fluids 29:465–483

Liu XN (2004) Gravel Bed Load Movement and Modeling, PhD Dissertation, Sichuan University, Chengdu, China (**in Chinese**)

Liu XN, Chen YX, Li H (1991) Study of near bed sediment movement by using high-speed photographing. Sediment Res 1:57–60 **(in Chinese)**

Liu F, Fu XD, Wang GQ, Duan J (2012a) Physically based simulation of dam breach development for Tangjiashan Quake Dam. China Environ Earth Sci 65:1081–1094

Liu HF, Li M, Shu AP (2012b) Large eddy simulation of turbulent shallow water flows using multi-relaxation-time lattice Boltzmann model. Int J Numer Meth Fluids 70:1573–1589

Pu JH, Cheng NS, Tan SK, Shao SD (2012) Source term treatment of SWEs using surface gradient upwind method. J Hydraul Res 50:145–153

Qian N, Wan ZH (1983) Sediment transport mechanics. Scientific Publishing, China (**in Chinese**)

Soares-Frazao S, Canelas R, Cao ZX, Cea L, Chaudhry HM et al (2012) Dam-break flows over mobile beds: experiments and benchmark tests for numerical models. J Hydraul Res 50(4):364–375

USACE (2003) HEC geospatial hydrological modeling extension user's manual, US Army Corps of Engineers, Research Center in Water Resources, University of Texas

Wang GQ (1999) Review of sediment issues in China. Adv Water Sci 3:337–344 **(in Chinese)**

Wang ZY, Song ZQ (1995) Review of sediment study in Europe and America. In: Proceedings of second national symposium on fundamental sediment theory. Beijing Construction and Material Industry Publisher, China, pp 3–15 (**in Chinese**)

Wang ZY, Zhang K (2012) Principle of equivalency of bed structures and bed load motion. Int J Sedim Res 27:288–305

Wang GQ, Liu F, Fu XD, Li TJ (2008) Simulation of dam breach development for emergency treatment of the Tangjiashan Quake Lake in China. Sci China Ser E Tech Sci 51(Supp II):82–94

Zhang RJ (1961) Alluvial dynamics. China Industry Publishing, China (**in Chinese**)

Zhang RJ (1998) Alluvial and sediment dynamics. China Hydraulic and Hydroelectric Publishing, China (**in Chinese**)

Zienkiewicz OC, Codina R (1995) A general algorithm for compressible and incompressible—flow. 1. The split, characteristic-based scheme. Int J Numer Methods Fluids 20:869–885